ELSEVIER

Journal of Nuclear Materials 296 (2001) 66–82

journal of nuclear materials

www.elsevier.com/locate/jnucmat

Determination of helium and hydrogen yield from measurements on pure metals and alloys irradiated by mixed high energy proton and spallation neutron spectra in LANSCE

F.A. Garner [a,*], B.M. Oliver [a], L.R. Greenwood [a], M.R. James [b], P.D. Ferguson [b], S.A. Maloy [b], W.F. Sommer [b]

[a] *Pacific Northwest National Laboratory, Materials Resources Department, 902 Battelle Boulevard, MSIN: P8-15, Richland, WA 99352, USA*

[b] *Los Alamos National Laboratory, Los Alamos, NM 87545, USA*

Abstract

The confident design of accelerator-driven spallation neutron devices will require good estimates of the cross-sections for generation of helium and hydrogen in the mixed spectra of high energy protons and neutrons that will be experienced by the structural materials. Improved estimates of these cross-sections were derived from a series of irradiations that were conducted at relatively low temperatures (<100°C) in the Los Alamos Neutron Science Center (LANSCE) as part of the test program supporting the Accelerator Production of Tritium (APT) Program. In this irradiation campaign, a variety of candidate structural alloys and pure metal dosimeter foils were irradiated in various particle spectra, ranging from 800 MeV protons, to mixed energy distributions of both protons and spallation neutrons, and finally to distributions consisting primarily of high energy neutrons. At proton energies on the order of hundreds of MeV, exceptionally high levels of gas atoms are generated in all elemental constituents of typical iron-based and nickel-based structural alloys, with helium typically on the order of ~150 appm per dpa and hydrogen at approximately a factor of 3–5 higher. Most of the gas production is due to proton and helium recoils from the proton beam interactions with the specimens, although gas and especially damage production from lower-energy spallation neutrons becomes increasingly significant at locations farther from the beam center. The results show that helium production rate per dpa by protons in elements typically found in structural alloys is relatively insensitive to elemental composition. The measured helium concentrations and the derived cross-sections are larger by about a factor of two, however, than those calculated using the LAHET code which was optimized for prediction of neutron/proton ratios in the target tungsten source rods of the APT test. Unlike helium, the retained hydrogen levels are somewhat sensitive to composition, reflecting primarily different levels of diffusional loss, but hydrogen is still retained at rather high concentrations, allowing a lower bound estimate of the hydrogen generation rates.

1. Introduction

Structural materials exposed to mixed spectra of high energy protons and lower-energy spallation neutrons found in accelerator-driven spallation neutron sources (SNS) must withstand the intensive generation and retention of large levels of helium and hydrogen. Confident prediction of these generation rates requires their measurement at high exposure, but very little data are available at high displacement dose levels. A recent irradiation series conducted at Los Alamos National Laboratory now provides the opportunity for such measurements.

The Accelerator Production of Tritium (APT) project [1] was proposed as one of several solutions to the US national need for tritium. In the APT concept, high-energy protons would impinge on a tungsten target producing high-energy spallation neutrons. These neutrons would in turn be multiplied using a lead blanket,

* Corresponding author. Tel.: +1-509 376 4136; fax: +1-509 376 0418.

E-mail address: frank.garner@pnl.gov (F.A. Garner).

0022-3115/01/$ - see front matter
PII: S0022-3115(01)00562-1

then thermalized in water. Tritium production would occur through capture of the thermalized neutrons by ^{3}He gas. An important technical issue that was addressed during the APT design was the potentially strong impact of radiation damage and transmutant production on structural materials resulting from the various mixed high-energy proton and neutron distributions expected in the APT facility.

A series of irradiations were conducted in the Los Alamos Neutron Science Center (LANSCE) as part of the experimental test program supporting the APT Program [2]. In this irradiation campaign, a variety of candidate structural alloys were placed in various particle spectra, ranging from 800 MeV protons, to mixed energy distributions of both protons and spallation neutrons, and finally to distributions consisting primarily of high-energy neutrons. The irradiation temperatures of specimens in the LANSCE test were 200°C or less, with most below 100°C, conditions expected to be typical of the APT facility.

At proton energies on the order of hundreds of MeV, exceptionally high levels of gas atoms are generated in all elemental constituents of typical structural alloys, with helium typically on the order of ~80–160 appm per dpa, and hydrogen (i.e., protium) at approximately an order of magnitude greater [3–5]. Whereas the generation of these gases in typical fission and fusion neutron spectra is very sensitive to elemental composition, especially the nickel content [6,7], there is very little difference expected between the rates of gas generation in nickel, iron or chromium at very high proton energies [5,6].

Proton energy spectra are composed of hydrogen that is born in two roughly equal distributions with very different birth energies, the first on the order of ~100 MeV in the internuclear cascade, and the second at ~1 MeV in the subsequent nuclear evaporation event. For typical specimen dimensions, the large range of the very high-energy protons produced in the internuclear cascade results in their near-total loss from the irradiated volume, while a significant fraction of the evaporation protons is stopped in the specimen. Thus, for in-beam specimens ~50% or less of the total generated hydrogen is expected to come to rest in the specimens. On the other hand, 90–95% of the heavier helium at lower energies is retained in specimens of the sizes employed in the APT irradiation program. (Actually, since all specimens in this experiment are covered by adjacent specimens and foil covers, helium fluxes across surfaces of adjacent pieces of metal should cancel, leading to little if any net loss.)

Since both of these gases are considered to exert a negative influence on structural properties of interest, their retention after both recoil and diffusional losses is of strong interest. Helium is essentially immobile in structural metals at all temperatures of nuclear interest, but hydrogen has some limited temperature-dependent mobility. To assess the degree of retention after both energetic and diffusional losses, each gas was measured in a number of highly irradiated specimens of different compositions and dpa levels.

The specimens chosen were of two types. The first were specimens of various alloys in the form of standard microscopy disks. The second type were dosimetry foils of pure metals. The radioactivation of these foils was used to characterize the proton and neutron spectra experienced by the alloy specimens.

2. Experimental conditions

A variety of structural alloys from the APT materials characterization program were analyzed for helium and hydrogen content, including Alloy 718, 300 series stainless steels (304L and 316L), and 9Cr–1Mo. Other alloys based on aluminum were included in the irradiation series but will be measured later in the program. There were a variety of specimen types irradiated in this experiment, but the gas measurements reported here for structural alloys were conducted on standard 3 mm disks used for transmission electron microscopy or shear punch studies.

In this paper we concentrate on alloy and dosimetry foil specimens irradiated primarily in the proton beam, although other specimens were also exposed primarily to lower fluxes of high energy neutrons, with the relative fraction of neutrons increasing toward the edge of the proton beam, as shown in Fig. 1. At the front of the experimental assembly the 1 mA proton beam was roughly Gaussian in distribution, with a 2σ of ~3 cm. The proton energy spectrum varies and changes with depth into the experimental assembly. Fig. 2 shows typical proton energy spectra for tubes 1 and 21, located in sections 17A and 18C of the experiment. A diagram of the experimental setup in the LANSCE facility showing these locations is depicted in Fig. 3.

A typical sample holder for TEM disks and other specimen types is shown in Fig. 4. The specimens are mounted in thin foil-covered blades with metal-to-metal contact for optimum cooling, with high velocity water flowing between the various blades. Proton-induced heating leads to somewhat higher temperatures at the higher dpa rates, however. Therefore, there is some coupling between dose and temperature, with the calculated temperature of the samples measured in this study rising from about 30°C at the lower doses to about 65°C in the beam center. This may induce some bias in the hydrogen retention data, tending to reduce it somewhat at higher dpa levels relative to that at the beam edges.

Alloy specimens measured in the current study were irradiated in a number of tubes located throughout the

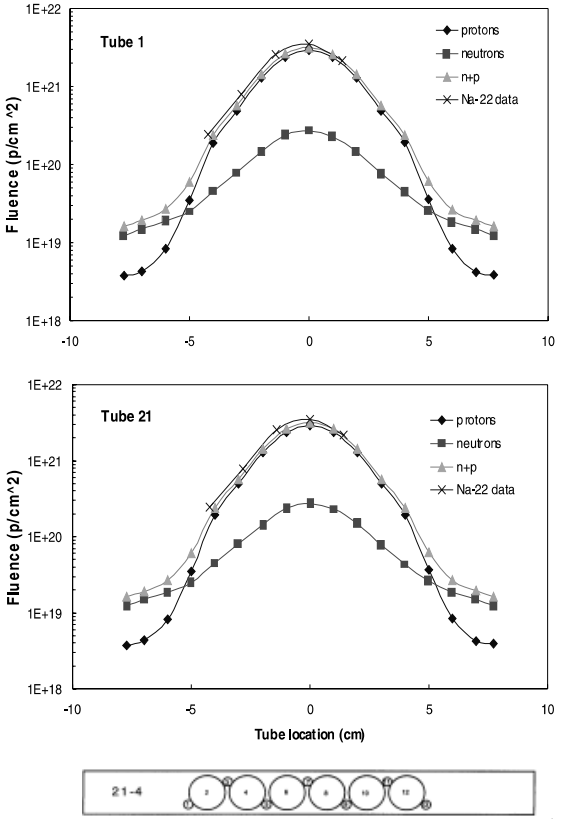

Fig. 1. Calculated vs. measured particle fluences for representative specimen tubes (numbers 1 and 21). Note that measured profiles shown above were determined using the Na-22 reaction in pure aluminum dosimeters included in the small dosimeter packets that were placed on each side of the specimens.

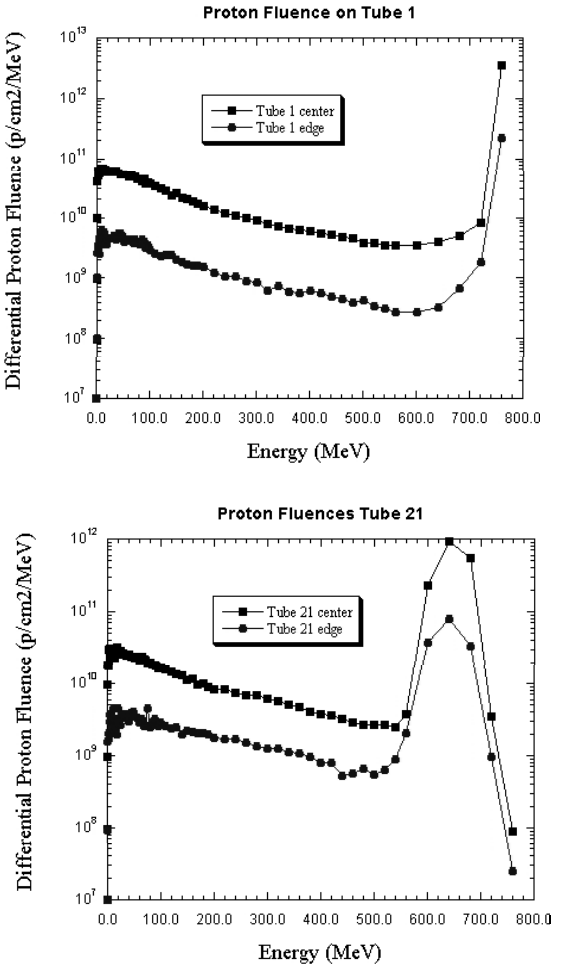

Fig. 2. Typical proton energy spectra for tubes 1 and 21, located in assembly 17A and assembly 18C of the APT experiment in LANSCE.

experiment. Some tubes such as number 21 were not directly centered on the beam axis, and therefore have profiles that are somewhat asymmetric in shape. The dosimetry foils chosen for measurement were irradiated in two positions in tube 21 at position 5 at −1.5 cm from the tube center, and position 13 at the edge of the specimen array at +5 cm. Thus these two packets had different relative amounts of proton and neutron fluxes, and different cumulative dpa levels, averaging ~0.8 and ~8 dpa, respectively, with the dpa levels depending slightly on the metal identity. Each foil pack contained six thin (0.05–0.4 mm) disks 3 mm in diameter, each of relatively pure metal, being Al, Cu, Fe, Co, Nb and Cu, stacked in that sequence with the protons impinging first on the Al foil, as shown in Fig. 5.

Details on the alloy samples measured for gas content are given in Table 1 and for the dosimeter foils in Table 2. Calculated helium and hydrogen contents based on the LAHET code system (LCS) [8] for each of the alloy specimens are also given in the last two columns of Table 1. The predicted hydrogen contents include energetic losses from higher energy protons, but do not include any estimate of diffusional losses. The calculated atomic displacement levels (dpa) were also determined by the LCS, averaging over all of the particles involved in the spallation reaction and using the standard NRT model [9]. The computational details and implications of these gas and dpa calculations will be explored later in the paper.

Specimens for gas analysis were cut from each original sample using small diagonal wire cutters in a controlled environment. Before each use, the cutters were cleaned by wiping several times with a dry 'Kimwipe'. Each of the helium analysis samples was etched to remove a minimum of ~0.013 mm (~0.5 mil) of surface material prior to specimen preparation. This etching step was performed to remove material that may have been affected by α-recoil either out of the sample or into the sample from adjacent materials during irradiation.

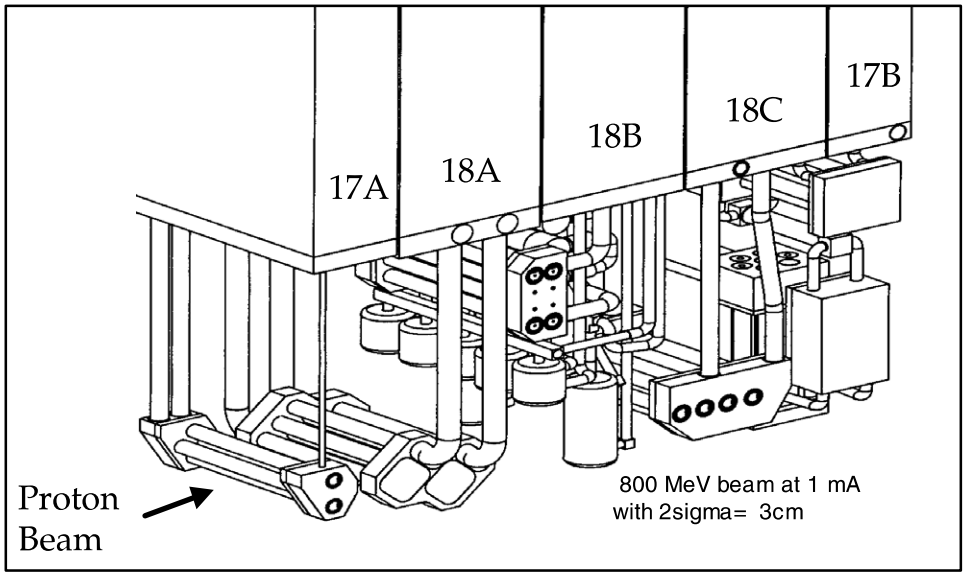

Fig. 3. APT irradiation set-up in the LANSCE Irradiation Facility. The specimens discussed in this paper were irradiated in assembly 17A (tube 21) and assembly 18C (tube 1).

After etching, two smaller specimens were cut from each sample for duplicate helium analyses. The hydrogen analysis specimens were cut in a similar manner from the un-etched original samples to avoid introduction of hydrogen.

Prior to analysis, each specimen was cleaned in acetone and air-dried. The mass of each specimen was then determined using a calibrated microbalance traceable to the National Institute of Standards and Technology (NIST). Mass uncertainty is estimated to be ±0.002 mg.

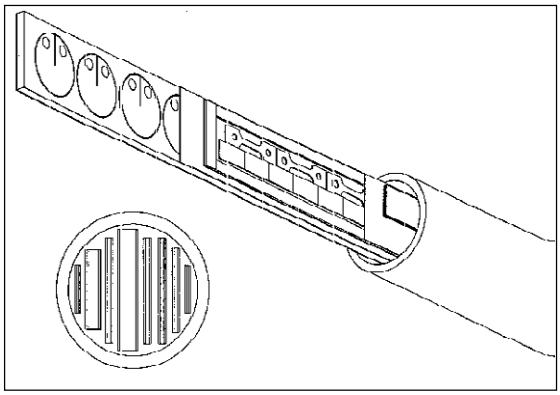

Fig. 4. Typical specimen holder containing many blades in the LANSCE irradiation series discussed in this paper. The various materials sit in specimen-shaped holes in 304 stainless steel plates, allowing metal-to-metal contact for good heat transfer. Each of these specimen holders was covered on both sides by a thin foil of 304 stainless steel. The blades were cooled by high velocity, flowing water with the inlet and outlet water temperature measured with thermocouples, allowing calculations of specimen temperature.

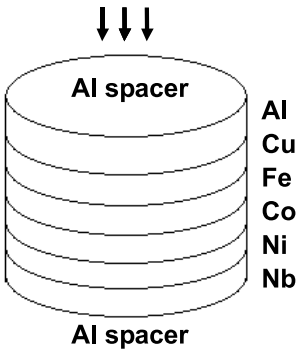

Fig. 5. Schematic of dosimeter foil packet loading and its relationship to the proton beam.

3. Helium analysis

3.1. Helium analysis system

Helium analyses were conducted by mass spectrometry at Pacific Northwest National Laboratory (PNNL). Details on the mass spectrometry system have been presented elsewhere [10,11]. Helium contents were determined by heating and/or vaporizing each sample in a resistance-heated crucible in one of the mass spectrometer system's high-temperature vacuum furnaces. The

Table 1
Alloy specimen summary

Sample	Material	Tube +No.[a]	Location[b] (mm)	Dose (dpa)	Calculated gas content[c] (appm)	
					Helium[d]	Hydrogen[e]
IN66	Alloy 718	21-2-1	−31.2	1.45	87.2	787.9
IN25		21-2-22	−31.2	1.45	87.2	787.9
INE4		21-2-11	10.0	3.87	252.1	2270
IN53		21-2-31	8.0	4.15	272.3	2446
INO1		1-1-7	−12	9.92	757.4	6603
IN43		1-1-10	0	13.77	1097	9544
4121	304L	22-2-12	8.0	3.82	243.3	2151
4077		4-2-11	0.0	9.77	695.1	5967
6138	316L	24-2-22	−31.2	1.34	74.4	657.8
6053		24-2-10	8.0	3.92	237.7	2101
6040		24-2-29	4.1	4.07	249.0	2207
6100		4-2-33	2.0	10.3	730.7	6246
MDC1	9Cr–1Mo	4-2-41	40.0	1.1	55.8	475.8
MD67		4-2-13	3.8	9.55	698.9	5905

[a] Tube-envelope-ID#.
[b] Location from beam centerline.
[c] Calculated using LCS.
[d] Includes both ^{3}He and ^{4}He.
[e] Includes energetic losses.

Table 2
Dosimetry specimen summary

Sample	Material and percent purity	Thickness (mil)	Foil stack	Protons (p/cm^2)	Dose (dpa)
C81	Al – 99.9974	5	1-5-13	1.58×10^{20}	0.67
C85	Cu – 99.9928	5			0.82
C82	Fe – 99.987	5			0.78
C83	Co – 99.896	2			0.80
C84	Ni – 99.837	3			0.82
C86	Al – 99.9974	5	1-5-5	2.47×10^{21}	3.5
C90	Cu – 99.9928	5			8.5
C87	Fe – 99.987	5			7.8
C88	Co – 99.896	2			8.3
C89	Ni – 99.837	3			8.5

concentrations of the two helium isotopes were determined either by direct measurements of the mass spectrometer signal for ^{3}He or ^{4}He, or by an isotope-dilution technique where the released helium is compared with a known quantity of added 'spike' of the other isotope.

The helium spikes were obtained by expanding and partitioning known quantities of gas through a succession of calibrated volumes [10]. The mass spectrometer was calibrated for mass sensitivity during each series of runs by analyzing known mixtures of ^{3}He and ^{4}He. Reproducibility of the analysis system for samples with known homogeneous helium content is ~0.5%. Absolute accuracy has been determined in many previous studies to be generally better than 1%.

3.2. Helium measurements in alloys

Helium analyses were conducted on a total of 14 alloy specimens from the APT materials tests. Some of the helium measurements on the Alloy 718 material included stepped-anneal analyses conducted to determine the extent of gas removal at temperatures up to ~1200°C, with examples of the helium release profiles of ^{3}He and ^{4}He shown in Fig. 6. These stepped-anneal analyses were followed by complete vaporization of the sample to completely remove the remaining helium. Because of eutectic formation of 718 with the crucible, resulting in premature sample melting, significant levels of helium were removed prior to 1200°C. Results of the

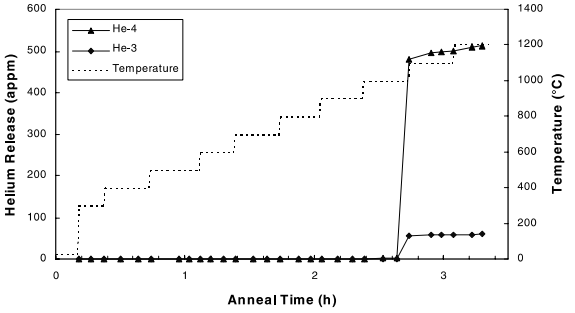

Fig. 6. Typical stepped-anneal helium release in Alloy 718. Abrupt helium release at ~1000°C is attributed to early melting caused by eutectic alloying of the specimen with the crucible.

various types of analyses agree well and are shown in Table 3 and graphically in Figs. 7–9. Note that the measurements in the figures include the total of ^{3}He and ^{4}He.

3.3. Helium measurements in pure metals

After counting of the radioactive isotopes to provide input for the flux-spectra determination, helium analyses were conducted on five of the six pure metal dosimeter foils in each of the two foil packets. The Nb foil in each pack could not be measured since it was earlier dissolved in order to count a soft X-rays from the decay of Nb-93 m. The results of the helium measurements of

Table 3
Measured helium in alloys

Sample	Material	Anal. Type[a]	Mass[b] (mg)	Measured helium					He/dpa[d]
				(10^{13} atoms)		(appm)[c]			
				^{3}He	^{4}He	^{3}He	^{4}He	Total	
IN66	Alloy 718	V	0.738	1.76	11.17	17.1	147	164	119
		V	1.027	2.59	17.19	18.8	162	181	±8
IN25		A	3.164	5.99	51.40				
		V		–	0.25	18.4	159	177	122
INE4		A	1.890	11.03	95.65				
		V		–	0.28	56.7	492	549	142
		A	1.356	8.11	68.38	58.0	490	548	±1
IN53		A	1.714	10.53	90.36				
		V		–	0.62	59.6	512	572	128
		V	1.074	5.731	48.62	51.8	440	492	±14
IN43		V	1.407	32.4	265.0	223	1829	2052	150
		V	0.900	21.2	170.4	229	1838	2067	±1
4121	304L	V	1.320	90.9	704.8	63.8	494.4	558	
4077		V	1.095	263	1868	220	1565	1785	186
		V	1.632	404	2869	227	1613	1840	±4
6138	316L	V	0.539	11.3	79.12	19.4	135.9	155	122
		V	0.710	16.4	114.1	21.4	148.8	170	±8
6053		V	0.271	14.4	110.9	49.2	378.9	428	107
		V	0.801	40.9	315.3	47.3	364.5	412	±3
6040		V	0.866	55.0	428.5	58.8	458.2	517	127
6100		V	1.451	385	2746	246	1752	1998	192
		V	1.287	329	2395	237	1723	1960	±3
MDC1	9Cr–1Mo	V	1.682	30.1	213.4	16.6	117.5	134	122
		V	1.551	27.6	195.7	16.5	116.8	133	±1
MD67		V	0.874	206	1462	218	1549	1767	182
		V	1.181	266	1911	209	1498	1707	±4

[a] Stepped-anneal (A) or vaporization (V) analysis.
[b] Mass of analysis specimen. Uncertainty is ±0.002 mg.
[c] Helium concentration in atomic parts per million (10^{-6} atom fraction) with respect to the total number of atoms in the specimen. Values for samples that were both stepped-anneal and vaporized is the total of the two analyses.
[d] Mean helium (appm) per dpa and 1σ standard deviation of replicate analyses.

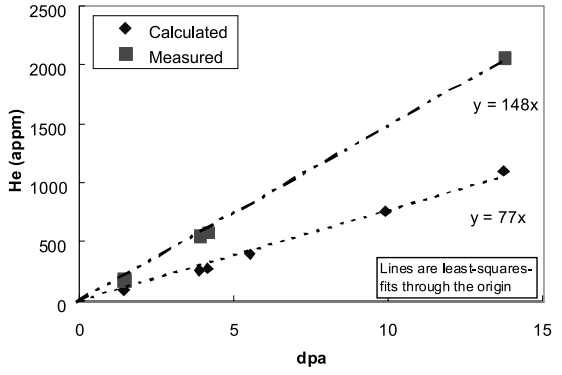

Fig. 7. Measured total helium in Alloy 718 vs. dpa. A comparison is made with the LAHET predictions.

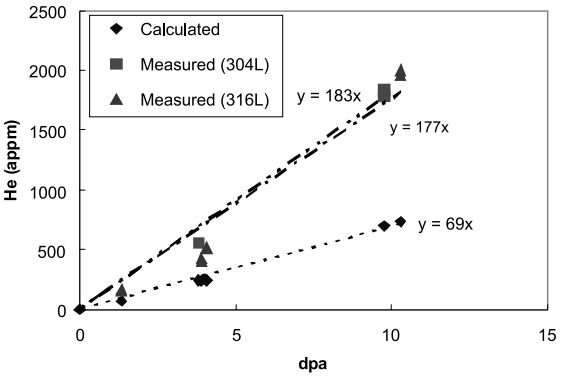

Fig. 8. Measured total helium in 300 stainless steels vs. dpa. A comparison is made with the LAHET predictions.

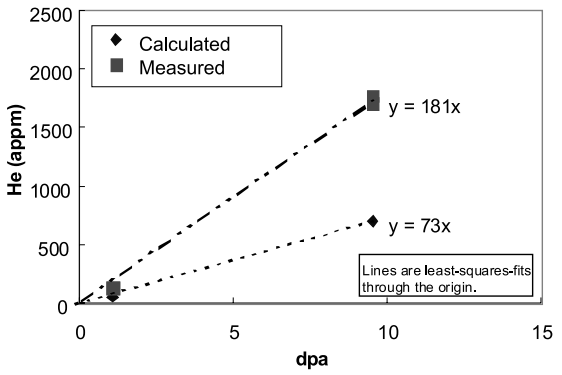

Fig. 9. Measured total helium in 9Cr–1Mo vs. dpa. A comparison is made with the LAHET predictions.

the pure metals are presented in Table 4 and plotted in Fig. 10. Note that with the exception of lower-Z aluminum, the He/dpa values of the four mid-Z elements quickly converge to values comparable to those of the alloys. The apparent failure of the two data sets at different dose levels to extrapolate to zero helium at zero dpa reflects the different contributions of neutrons and protons to both dpa and gas generation.

The Al results at higher He/dpa rates at first may seem surprising since lower-Z elements are known to produce somewhat less helium per incident proton. However, the partition of energy loss between nuclear and electronic stopping modes is also very different for low-Z materials. In aluminum the electronic loss fraction is much larger, producing less nuclear stopping and therefore much less dpa. The higher He/dpa rate for aluminum therefore reflects more the lower dpa production per proton than the moderate decrease in helium production with smaller atomic number.

4. Hydrogen measurements

4.1. Hydrogen analysis system

Hydrogen analyses were conducted using a newly developed analysis system at PNNL. Details of the system have been presented elsewhere [12]. The system is based on a low-volume extraction furnace in combination with a quadrupole mass spectrometer, and has a detection limit of ~1 appm for steel. Samples for analysis are loaded into the sample holder carousel located above the extraction furnace. Sample analyses are conducted by sequentially dropping the individual specimens into the heated crucible. Hydrogen release, in terms of current output from the electron multiplier, is measured as a function of time. Total hydrogen released is determined from the integral of the hydrogen release curve and the measured system sensitivity. Note that deuterium and tritium were not measured as LAHET calculations indicate very low generation rates of these isotopes compared to protium.

Measurements of hydrogen release with temperature were also made on a few samples of Alloy 718. These measurements were made while ramping the crucible temperature in an approximately linear profile from about 250–1200°C over a 400 s time period. The temperature profile was determined following the measurements using a thin-walled K-type thermocouple inserted from the upper sample loading area.

Calibration of the system was accomplished using a hydrogen leak source attached to the vacuum line between the extraction furnace and the detector volume. This calibrated leak has a very small trapped volume, resulting in virtually no lowering of the leak rate with time. Calibration measurements are conducted before and after each sample analysis, and typically show an overall standard deviation of ~2–3% for each analysis series. The system has been determined to be linear up to a total hydrogen release of at least 10^{17} atoms, which for

Table 4
Measured helium in dosimetry foils

Sample	Material	Mass[a] (mg)	Measured helium						
			(10^{14} atoms)		He^3/He^4 ratio	(appm)[b]			He/dpa[c]
			He^3	He^4		He^3	He^4	Total	
C81	Al	0.135	0.299	2.306	7.70	9.93	76.56	86.49	132
		0.177	0.417	3.184	7.64	10.4	79.73	90.13	±4
C82	Fe	0.424	0.820	3.879	4.73	17.9	84.87	102.2	128
		0.667	1.22	5.829	4.76	17.0	81.07	98.07	±4
C83	Co	0.120	0.168	1.139	6.77	13.7	92.87	106.6	134
		0.236	0.335	2.264	6.76	13.9	93.87	107.8	±1
C84	Ni	0.286	1.23	3.198	2.61	41.9	109.0	150.9	173
		0.692	2.78	6.693	2.41	39.2	94.27	133.5	±11
		0.200	0.833	2.065	2.48	40.6	100.6	141.2	
C85	Cu	0.530	0.514	4.100	7.98	10.2	81.63	91.83	123
		0.720	0.811	6.524	8.04	11.9	95.61	107.5	±10
		0.362	0.392	3.135	7.99	11.4	91.38	102.8	
C86	Al	0.340	10.5	76.27	7.28	138	1005	1143	325
		0.398	11.4	82.76	7.29	128	932	1060	±17
C87	Fe	0.502	10.1	66.03	6.51	187	1220	1407	180
		0.636	12.7	83.62	6.58	185	1220	1405	±1
C88	Co	0.266	4.69	33.99	7.25	173	1250	1423	169
		0.390	6.72	48.58	7.23	169	1219	1388	±3
C89	Ni	0.207	3.94	26.53	6.74	186	1249	1435	167
		0.407	7.53	50.88	6.76	180	1218	1398	±3
C90	Cu	0.882	12.4	97.32	7.82	148	1164	1312	152
		1.273	17.6	136.6	7.76	146	1132	1278	±3

[a] Mass of analysis specimen. Mass uncertainty is ±0.002 mg.
[b] Total helium concentration in atomic parts per million (10^{-6} atom fraction) with respect to the total number of atoms in the specimen.
[c] Mean helium (appm) per dpa and 1σ standard deviation of replicate analyses.

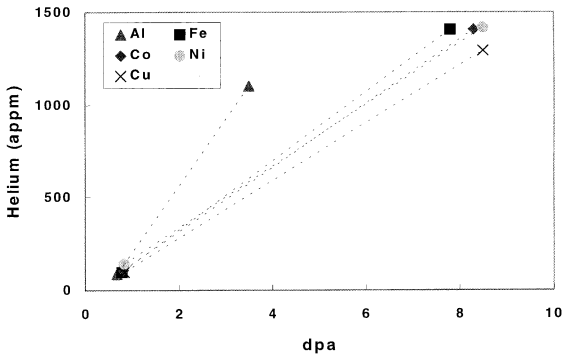

Fig. 10. Measured total helium in pure metal dosimeter foils.

a 0.5 mg steel sample, represents a hydrogen concentration of ~20 000 appm.

Measurements are also routinely conducted on specimens of a standard, hydrogen-containing steel maintained in the laboratory. The stated content of the steel is 5.2 ± 0.3 wppm. The average hydrogen content measured in more than 90 specimens ranging in mass from ~2 to ~8 mg is 5.0 wppm with a standard deviation of ~20% (1σ). It is speculated that the variability observed in the standard samples is associated with actual heterogeneity in the hydrogen content at this small mass level.

4.2. Retained hydrogen in alloys

Hydrogen measurements were made on a total of 13 samples from the APT materials characterization tests, and on unirradiated control samples of the same materials. The results of the control analyses are given in Table 5; the retained hydrogen levels measured in the irradiated materials are shown in Table 6. The hydrogen results are shown graphically in Figs. 11–13. The mean and standard deviation of the replicate measurements

Table 5
Hydrogen in unirradiated alloys

Sample	Material	Mass (mg)[a]	Measured hydrogen (10^{15} at.)	Hydrogen concentration	
				(appm)[b]	Mean[c]
In-bulk	Alloy 718	1.931	3.45	174	190
		2.014	4.14	200	±20
304L-blk	304L	3.824	13.3	319	320
		4.940	17.2	320	±0
316L-blk	316L	3.014	11.7	360	448
		3.844	22.2	535	±124
9Cr–1Mo-blk	9Cr–1Mo	2.821	1.94	64	58
		4.089	2.30	52	±8

[a] Mass of specimen for analysis. Mass uncertainty is ±0.002 mg.
[b] Hydrogen concentration in atomic parts per million (10^{-6} atom fraction) with respect to the total number of atoms in the specimen.
[c] Mean and standard deviation (1σ) of duplicate analyses.

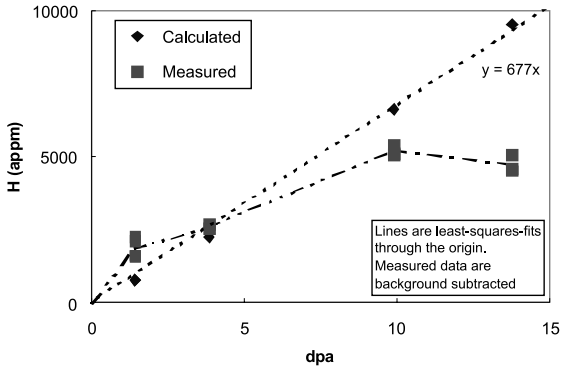

Fig. 11. Retained hydrogen in Alloy 718 vs. dpa, compared with LAHET prediction.

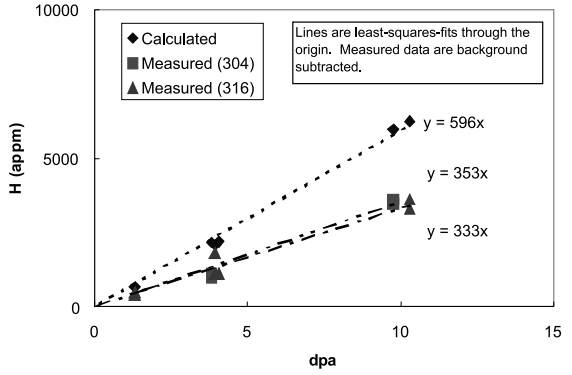

Fig. 12. Retained hydrogen in 300 stainless steels vs. dpa, compared with LAHET prediction.

are given in the last two columns of the table. The data in the last two columns of the Table 6 represent the 'net' hydrogen retained in the samples after subtraction of the measured hydrogen in the unirradiated materials. Absolute uncertainty (1σ) in the hydrogen analyses is estimated at ~20%, and is due partly to the uncertainty in the calibrated hydrogen leak source discussed above. Additional uncertainty may also be present from possible hydrogen release from remaining water layers or hydrated metal oxides on the surface of the sample that are subsequently dissociated by the hot crucible.

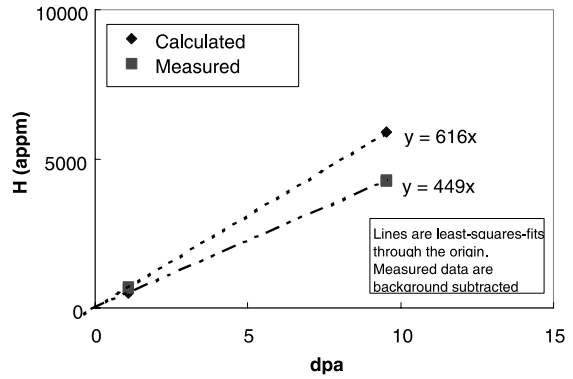

Fig. 13. Retained hydrogen in 9Cr–1Mo vs. dpa, compared with LAHET prediction.

4.3. Retained hydrogen in pure metals

Comparable information on hydrogen measurements in pure metals is given in Tables 7 and 8, and is plotted in Fig. 14. Note that the retained hydrogen varies rather strongly with the metal studied. The differences in hydrogen retention do not follow the known trends related to solubility or diffusion of hydrogen in various metals and alloys, and probably reflect different trapping types and densities induced by radiation in each alloy or metal.

The low exposure foils in general have higher retained He/dpa ratios than the high exposure foils. This is thought to be produced by lower energy protons being more easily retained due to the low kinetic energy of the hydrogen when it is produced by lower energy neutrons

Table 6
Retained hydrogen in alloys

Sample	Material	Mass (mg)[a]	Measured hydrogen (10^{15} at.)	Hydrogen concentration (ppm)[b]		
				Measured	Corrected[c]	Mean[d]
IN66	Alloy 718	1.639	30.7	1820	1630	1870
		2.366	56.0	2300	2110	±340
IN25		0.587	10.6	1760	1570	1810
		0.509	9.41	1790	1600	±380
		0.683	17.2	2440	2250	
INE4		1.059	29.7	2720	2530	2600
		0.732	21.6	2860	2670	±100
IN01		0.342	19.7	5590	5400	5200
		0.693	37.9	5310	5120	±180
		0.539	29.2	5260	5070	
IN43		2.386	117	4750	4560	4710
		1.912	103	5250	5060	±300
		1.328	64.3	4700	4510	
4121	304L	1.215	17.3	1300	980	1050
		2.336	37.0	1450	1130	±110
4077		1.806	78.0	3960	3640	3560
		0.955	39.7	3810	3490	±110
6138	316L	1.126	10.7	882	434	459
		1.305	13.1	932	484	±35
6053		1.283	21.6	1560	1110	1460
		1.741	42.4	2260	1810	±490
6040		2.407	40.4	1550	1100	1100
		3.497	58.8	1560	1110	±10
6100		1.391	61.0	4060	3610	3460
		1.030	41.8	3760	3310	±210
MDC1	9Cr–1Mo	1.071	85.0	735	677	687
		1.580	12.9	754	696	±13
MD67		1.910	89.5	4340	4280	4260
		2.050	95.2	4300	4240	±30

[a] Mass of specimen for analysis. Mass uncertainty is ± 0.002 mg.
[b] Hydrogen concentration in atomic parts per million (10^{-6} atom fraction) with respect to the total number of atoms in the specimen.
[c] Corrected for hydrogen in unirradiated controls (see Table 3).
[d] Mean and standard deviation (1σ) of duplicate analyses.

or possibly by synergism of efficient displacement production combined with low energy proton production.

5. Discussion: helium generation

Due to the short range of alpha particles, cross-surface interactions between neighboring specimens and the manner in which the helium content of the specimens were measured, it is certain that the measured values represent the generation rates without significant loss. The most significant observation from these studies is that the measured helium generation rates are significantly higher than expected based on LAHET calculations. This is a rather general problem as demonstrated in a compilation by Enke et al. [13] who showed that helium cross-section measurements for Fe and Ni over a wide range of monoenergetic energies were larger than predicted by the INCL, LCS and HERMES code systems.

As is evident in Figs. 7–9, helium generation rates per dpa appear to be the highest for the iron-based alloys (300 series stainless steels and 9Cr–1Mo) at ~180 appm/dpa. The lines through the measured data in the figures are least square fits assuming linear behavior through the origin, an assumption to be addressed in more detail

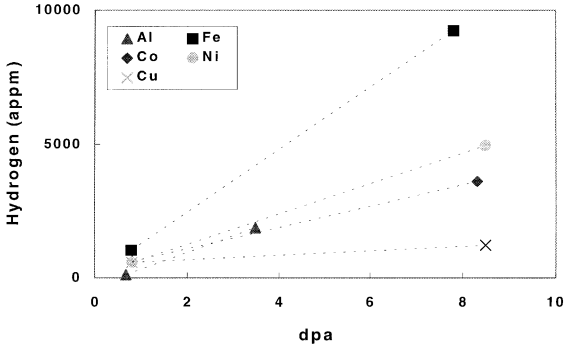

Fig. 14. Measured hydrogen in pure metal dosimeter foils.

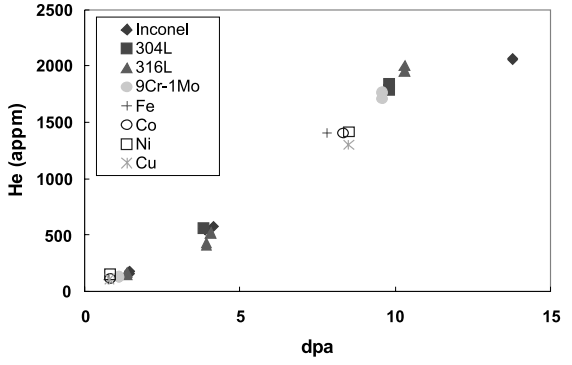

Fig. 15. Summary plot of measured helium in all alloys and pure metals with the exception of pure aluminum. Note that the highest data point for Alloy 718 tends to lie below the trend established by the other data, casting some uncertainty on the dpa assignment for this datum.

shortly. Helium generation in nickel-base Alloy 718 appears to be slightly lower at ~150 appm/dpa. It is important to note, however, that the difference between nickel-based and iron-based alloys may not be the only or dominant factor, since 718 also contains a rather high level (~8 wt%) of high atomic weight elements Mo, Nb, and Ta, while the iron-based alloys have Mo at only 0.3–2 wt%.

It is very significant, however, that the measured helium generation rates of pure Fe and pure nickel at the high exposure of ~8 dpa are 180 and 167 appm per dpa, remarkably close to the values of the two alloy groups. Both of these data sets involve mixed proton–neutron exposure. These measurements are also in relatively good agreement with that of earlier irradiations also conducted at LANSCE with essentially monoenergetic 750 MeV protons by Green et al. [14]. They measured He/dpa ratios of 169 and 158 appm/dpa in pure iron and pure nickel, respectively. As will be shown later, the difference between the results of Green et al., and the current results are even smaller when compared only on proton contributions.

In addition to the relatively small variations arising from composition differences, it is important to recognize that the measured helium concentrations in the current study are the result of generation rates averaged over a distribution of proton energies. It is also important to note that the relative contributions of neutrons to gas generation and displacement production also vary across the beam. Compared to protons, lower-energy spallation neutrons are more efficient to create displacements but less efficient to create gas. Thus, at progressively lower dpa levels with increasing neutron contributions, it is expected that the helium/dpa ratios of the mixed particle spectra should become smaller. In spite of these inherent biases in the data set, the measured concentrations are nearly linear with dpa and roughly independent of composition. This latter point is particularly demonstrated in Fig. 15, where the measured helium data in all the alloys and pure metals are summarized on a single plot.

Table 7
Hydrogen in pure metal dosimetry foils (unirradiated controls)

Specimen	Analysis temperature[a] (°C)	Mass[b] (mg)	Measured hydrogen	
			(10^{15} atoms)	(appm)[c]
Al	600	0.700	1.07	69
		0.591	1.49	113
Fe	1200	1.512	2.17	133
		2.125	3.35	146
Co	1200	0.920	1.95	207
		0.913	1.53	164
Ni	1200	1.232	1.56	124
		1.322	1.34	99
Cu	870	1.848	2.73	156
		1.712	1.21	75

[a] Temperature of system crucible.
[b] Mass of specimen for analysis. Mass uncertainty is ±0.002 mg.
[c] Hydrogen concentration in atomic parts per million (10^{-6} atom fraction) with respect to the total number of atoms in the specimen.

Table 8
Retained hydrogen in APT dosimetry foils

Specimen	Material	Analysis temp.[a] (°C)	Mass[b] (mg)	Measured hydrogen	
				(10^{15} atoms)	(appm)[c]
C81	Al	600	0.475	2.27	214
			0.552	2.86	232
C82	Fe	1200	2.062	25.4	1140
			1.641	21.5	1210
C83	Co	1200	0.817	6.79	813
			1.281	10.4	790
C84	Ni	1200	1.098	36.0	3190
			1.254	39.1	3040
C85	Cu	870	0.948	4.87	330
			1.408	14.2	1060
C86	Al	600	0.322	14.3	1990
			0.538	23.0	1920
C87	Fe	1200	1.717	235	12 700
			1.920	150	7270
			1.107	60.7	5080
			1.323	177	12 400
C88	Co	1200	0.610	16.5	2640
			0.766	45.9	5870
			0.575	19.7	3360
			0.629	20.9	3260
C89	Ni	12000	0.828	54.9	6460
			1.246	61.2	4780
			0.738	31.7	4190
			0.838	41.7	4850
C90	Cu	870	1.001	13.2	1390
			1.168	14.4	1300

[a] Temperature of system crucible.
[b] Mass of specimen for analysis. Mass uncertainty is ±0.002 mg.
[c] Hydrogen concentration in atomic parts per million (10^{-6} atom fraction) with respect to the total number of atoms in the specimen.

Note that all data points except that of Alloy 718 at 13.8 dpa clearly exhibit one behavior, suggesting that the dpa assignment for this specimen might have been in error. If the actual dose was 11.6 dpa, this datum would fall onto the trend line of the other data. This would also raise the helium/dpa value shown in Fig. 7 to ~176 appm/dpa, comparable to that of the two iron-based alloys.

Fig. 16 shows that for materials in the proton beam, the calculated He/dpa ratio remains relatively constant across the beam. It is towards the beam tails, where the neutron contribution becomes significant, that the ratio will change. The He/dpa ratio is also relatively independent of composition, particularly in-beam. As the relative neutron fluence becomes significant compared to the proton fluence there are two consequences, both of which act to decrease the local He/dpa ratio. First, the spectrum-averaged helium cross-section decreases, and second, the relative neutron contribution to the dpa rate increases. For these reasons, the measured helium levels at low dpa levels tend to lie slightly below the linear lines drawn in Figs. 7–9. In all cases, however, the measured helium levels are considerably higher than those calculated by LAHET, as shown in Figs. 7–9.

Where might this persistent tendency to under-prediction arise? The calculated production rates for both He and H were generated using the LCS [8], version 2.83. In this version the Bertini intra-nuclear cascade model was used with the pre-equilibrium option turned on. The level density model used was that of Gilbert–Cameron–Cook–Ignatyuk (GCCI) [15,16].

The LCS is the neutronic tool used for the design of APT and for the estimation of radiation damage parameters, such as dpa and gas production. The physics options employed in LAHET as the standard APT settings were chosen primarily to provide the proper n/p

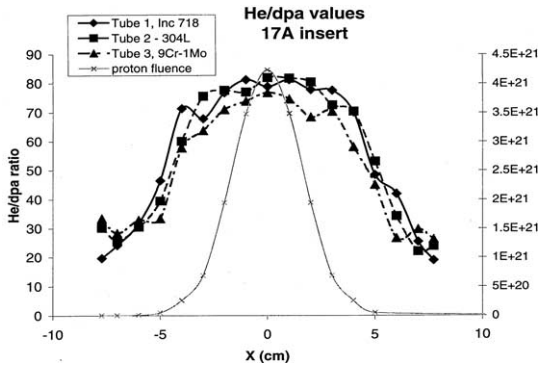

Fig. 16. LAHET-calculated He/dpa ratios for several alloys irradiated in different blades of insert 17A, showing that even though the proton fluence falls strongly and the energy and particle spectra change with position, the calculated He/dpa ratio remains relatively constant until the neutron contribution to the total fluence becomes relatively large near the edges of the proton beam.

ratios for high-Z targets such as tungsten, since tungsten rods are the target in APT. Using these options the accuracy in He production for mid-Z (~20–40) elements is known to be low by about a factor of two [15].

It is worth noting that LCS calculations for helium production in tungsten in this irradiation series agree well with measured data, as shown by Oliver and coworkers in a companion paper [17]. This implies that the current calculations do not under-predict He production for all Z, but for just an intermediate range of Z. Since the physics options were chosen to provide the proper n/p ratios for tungsten, the improved prediction of He/p is therefore not too surprising.

Interestingly, Green's earlier study [14] used HETC, a predecessor to LCS, to calculate the dpa levels and gas contents for a wide range of atomic numbers. While HETC used physics models similar to LCS, the exact parameter settings used for the calculations can vary significantly within 'reasonable' ranges, so it is not known to what degree the calculational methods agree. While Green's HETC-calculated values agreed with her measured values for pure iron and nickel, her calculations for helium production in tungsten were high by a factor of almost three when compared to the measured results. Unfortunately, it is not known what physics settings were employed in the then-current version of HETC used by Green. These different results indicate that neither the model used by Green nor the current LCS physics models are accurate for the prediction of helium production in all materials. User knowledge of the calculational models and of data in the field are critical in determining a He production value that can be believed better than a factor of two.

The measured helium 4/3 ratios may provide an independent opportunity to assist in the benchmarking of the LCS. For both neutrons and protons, He-4 is always easier to make than He-3. He-3 has a higher energy threshold meaning that as the spectral energy decreases, the ratio of He-4/He-3 should increase. However, other factors are also involved.

As expected, significant levels of ^{3}He were also measured in the various alloys and also in the pure metals. Lower energy neutrons produce very little ^{3}He and therefore protons should produce most of the ^{3}He. Measured ^{4}He/^{3}He ratios varied from 7.0 to 8.6 in the alloys, and showed little variation with dpa level in the range of 1–14 dpa. The helium 4/3 ratios were the highest for Alloy 718, and appear to scale with the level of high-Z components in the material rather than with the major components Fe or Ni.

Previous measurements in LANSCE by Green et al., for higher-Z pure materials irradiated with 750 MeV protons [14] showed higher helium 4/3 ratios (Fe, 8.66; Ni, 8.16; Cu, 9.44; Mo, 10.1; W, 13.7; Au, 11.4), indicating that high-Z materials indeed tend to increase the 4/3 ratio.

The pure metals at the highest exposure in this experiment (~8 dpa) also had comparable helium 4/3 ratios for pure iron and nickel at 6.6 and 6.7, respectively, but these are somewhat lower than those of Green at 8.86 and 8.16 [14]. These relatively small differences may reflect some aspect of the energy spectra, remembering that Green's study used essentially monoenergetic protons with very little neutron contribution.

One surprising result of this study is that the helium 4/3 ratios of Fe and Ni at the lowest exposure of 0.8 dpa were significantly lower at 4.7 and 2.5, respectively. The reasons for this result are not yet understood. However, the increase in 4/3 ratios from 0.8 to 8 dpa in this mixed spectra experiment, and then to the higher values of Green's monoenergetic proton study is suggestive of two possible interpretations. First, there may be an increase of the He 4/3 ratio with increasing proton energy, and second, there may be an unsuspected ^{3}He contribution from neutrons. The authors favor the first interpretation, noting that the mean proton energy decreases when moving from Green's experiment through the mixed spectra experiments toward lower dose.

The other pure metals (Al, Co, Cu) had helium 4/3 ratios of 7.3, 7.2 and 7.8, respectively, at the higher exposure level of ~8 dpa. The values at the lower exposure of 0.8 dpa were remarkably similar at 7.7, 6.8 and 8.0, all well within experimental error. In these cases, it is not necessary to invoke any dependence of the ratio on mean proton energy.

6. Discussion: hydrogen generation and retention

As shown in Fig. 17, the calculated H/dpa generation ratio in this experiment remains relatively independent

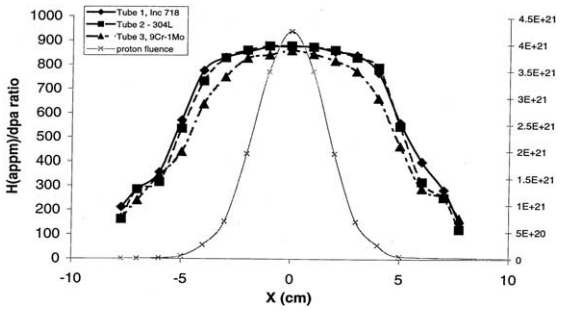

Fig. 17. LAHET-Calculated H/dpa ratios for several alloys irradiated in different specimen blades of insert 17A, showing that even though the proton fluence falls strongly and the energy and particle spectra change with position, the calculated H/dpa ratio remains relatively constant until the neutron contribution to the total particle fluence becomes relatively large near the edges of the proton beam.

of both alloy composition as well as proton energy and spectral variations. The calculated H/He ratio is also known not to change strongly as a function of proton energy in the energy range relevant to this experiment [4]. Hydrogen in this case is considered to be only protium, since deuterium and tritium were not expected to be generated at large rates compared to protium and were not measured.

The data in Figs. 11–13 are the net retained hydrogen after subtraction of the measured hydrogen in the unirradiated materials. As with helium, the retained hydrogen in the 300 series steels and 9Cr–1Mo scale approximately linearly with dpa, but at a higher rate of ~600 appm/dpa. Remember, however, that the inherent bias in temperature with dpa rate may lower this retention rate per dpa somewhat relative to that in a fully isothermal experiment.

Alloy 718, however, showed a marked non-linearity in the retained hydrogen, with three trend lines shown in Fig. 11 with progressively lower slopes, a relatively higher rate in the first dose interval from 0 up to ~1.5 dpa, a second lower rate from ~1.5 to ~10 dpa, and a third, possibly negative rate above ~10 dpa.

The complex hydrogen behavior observed in Alloy 718 is attributed to a rather complex microstructural evolution that occurs in this alloy compared to that of the other alloys. According to Sencer et al. [18], the radiation-induced microstructural evolution in the three iron-base alloys was rather simple, involving only the nucleation and growth of small faulted Frank loops and smaller 'black spots'. Therefore, these microstructural defects probably serve as the only available trapping sites for hydrogen, with the possible exception of He/H complexes in the matrix. (Sencer did not observe any cavities down to a resolution limit of ~1 nm.)

In Alloy 718, however, Sencer observed that the starting microstructure was composed of a high density of very small, ordered γ' and γ'' precipitates, whose surfaces could serve as trapping sites along with the developing faulted loops and black spots. With increasing damage levels, however, the precipitates were first disordered and then their elemental constituents were progressively mixed back into solution. Again, no resolvable cavities were observed, even though a total gas content approaching 0.7 at.% was reached at the highest dpa level. Such a scenario might explain the initially high and then progressively lower hydrogen storage rate with increasing dpa level observed in Alloy 718.

Contrary to the behavior observed in the helium concentration, the calculated hydrogen values generally over-predict the measured hydrogen content. The possible exception is the initial slope observed in the Alloy 718 up to ~1.5 dpa, where the highest trapping efficiency was postulated. It should be noted that the calculated hydrogen generation is relatively insensitive to alloy composition, so only microstructural differences in diffusion can account for the lower and rather divergent hydrogen levels in the various alloys. Given the uncertainties in the calculated energetic losses and the lack of knowledge of diffusional losses, this over-prediction is not unexpected, since hydrogen losses must be occurring.

There may be some bias in several of the hydrogen measurements in the dosimeter foils, however. Note in Fig. 5 that there are significant differences in atomic number of adjacent specimens in two cases, Al/Cu and Ni/Nb. Since the spallation-produced protons have larger ranges than do alpha particles and proton generation is sensitive to atomic number, there is a higher probability of 'cross-talk' between specimens, leading to some skewing of the retained hydrogen that is not related to solubility.

It is somewhat surprising that so much hydrogen is retained in these metals and alloys. The most significant observation is that the differences between calculated and measured values are not very large if recoil and diffusional losses of up to 50% are assumed for the temperatures involved in this experiment. Since proton production in LAHET is treated as a primary reaction channel, one would expect a better ability to predict hydrogen generation compared to that of helium, which is considered to be a secondary channel with more inherent calculational uncertainty. Although no attempt has been made here to account for diffusional losses, estimates of the average hydrogen diffusion length for the current irradiation conditions (i.e., ~30–100°C for 180 days) would suggest that, in the absence of defect trapping, even at the lower temperatures, most of the generated hydrogen should have been lost. Therefore, trapping of the hydrogen at defect clusters and possibly helium sites may play a significant role in the hydrogen retention. Also, the rate of hydrogen production rises

with energy, but trapping does not, again suggesting the radiation damage is the controlling factor.

Our best conclusion might be that H retention depends less on the production of H than on the production of damage. This might mean for some systems (e.g., SNS) where there are large contributions to dpa from neutrons, that the H/dpa ratio might still be very high. In other words, the H is produced primarily by the proton beam, but trapped more efficiently by the neutron-induced damage.

7. Application of these data to other spectral environments

Before these data can be applied to other spectral environments such as the SNS [3], it is necessary to further decouple the neutron and proton contributions to both the gas generation and the production of displacement damage. In the current experiment, for instance, the major source of the neutron flux is the tungsten rods in the 18A portion of the assembly, as shown in Fig. 3, rather than the structural material itself. This separation between source and structural material tends to dilute the relative neutron contributions to the total damage and gas generation.

More significantly, the SNS target is compact and range thick for 1 GeV protons, in contrast to the LANSCE irradiations where a significant amount of the proton beam passed though the assemblies to the beam stop. Additionally, the front surface of the SNS target, is adjacent to the liquid mercury and therefore in more intimate contact with the neutron source. Thus one should anticipate that the calculated gas generation rates per dpa would be significantly lower in SNS than in the current experiment.

While the neutron contributions to displacement production and gas generation are reasonably well known, this paper has shown that the proton-induced contributions must be better described, and by experiment rather than calculation. Once proton cross-sections are measured then the input assumptions to LAHET can be modified to better describe the local material environment.

In order to apply the measurements made in this experiment to other spectral environments, one must first attempt to remove the neutron contributions from the measurements. Second, one must address the potential difference in proton energy distribution between the APT experiment and the other environment. In both cases we can use LAHET to provide estimates of the necessary parameters.

Figs. 18 and 19 show LAHET calculations of the fractional contributions of neutrons to the dpa and gas generation rates. Noting that ~180 appm/dpa helium was generated in the three iron-rich alloys, we can see that neutrons contributed ~16% to the dpa and only about 2% to the helium production in the middle of the beam where the proton contribution was the greatest. Thus the proton-induced contribution to helium production was $\sim 180 \times 0.84/0.98$ or ~154 appm/dpa in iron-rich Fe–Ni alloys. Remember that Green measured 169 and 158 appm/dpa for Fe and Ni for 750 MeV protons [14], but we are uncertain what input parameters were used in Green's study to calculate gas generation. Since LAHET underestimates proton gas production by about a factor of two, the 2% neutron contribution would decrease to about 1%, not a big change, assuming that the dpa production was correctly calculated.

This helium was produced over a range of proton energies, ~500–800 MeV. However, an energy-depen-

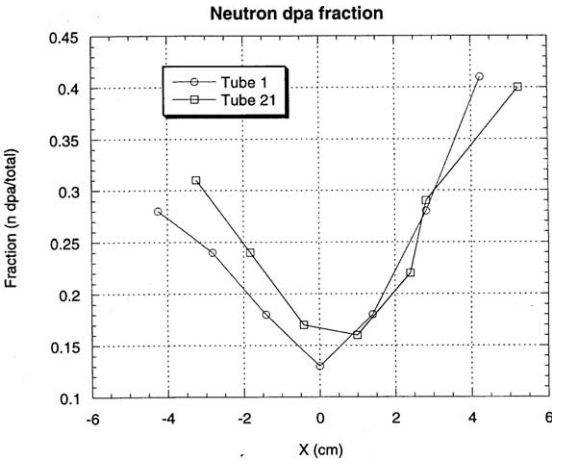

Fig. 18. Fractional contribution to atomic displacements from neutrons in this experiment, as calculated by LAHET.

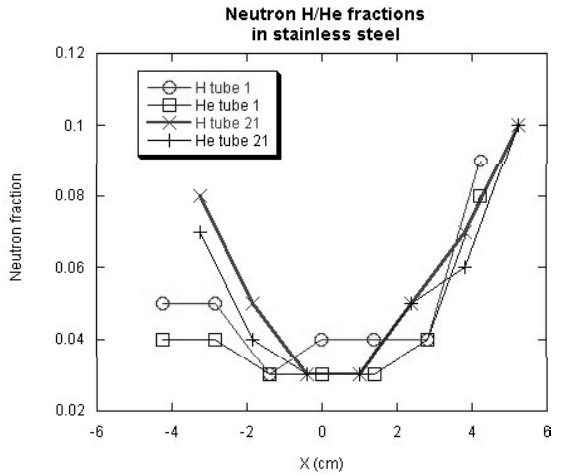

Fig. 19. Fractional contribution to gas generation from neutrons in this experiment, as calculated by LAHET.

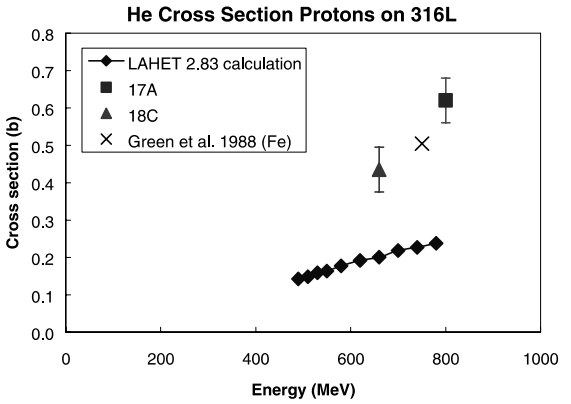

Fig. 20. Comparison of energy-dependent cross-sections for helium production derived from this study with those predicted by LAHET.

dent cross-section in barns is needed. Fig. 20 shows our estimation of the energy-dependent cross-section for proton-induced generation of helium in 316 stainless steel, with the LAHET prediction shown for comparison. Fig. 20 was generated by first extracting the component of He that was produced by the protons. This is possible because activation foil analysis provides the relative proton and neutron spectra and this is combined with the gas production cross-sections calculated with LCS. The average energy of the protons changed as inserts attenuated the beam, so two different beam conditions can be studied. The samples in 18C saw a proton beam of average energy around 660 MeV (and with a greater peak width) than the 17A samples which saw a nearly mono-energetic proton beam at 800 MeV. The results clearly show for 316L the rising He production with energy that also agrees well with the data from Green et al. [14] for pure Fe. The LAHET calculations are also shown and they clearly exhibit the discrepancies in both yield and energy dependence.

Although LCS helium production calculations for iron are known to agree well with experimental data near 20 MeV, the clear and growing discrepancy in the calculated and measured cross-section for the proton energies covered in this experiment indicates that using LCS to calculate helium production in mid-Z materials for new systems at higher energies (e.g., SNS, ESS, etc.) is not advised in the absence of experimental data.

8. Conclusions

This study has shown that helium generation rates in typical iron-base and nickel-base alloys are very insensitive to alloy composition during irradiation with protons in the 500–800 MeV range, especially when concurrent neutron fluxes are relatively smaller. The helium generation rates of mid-Z elements are measured to be larger by roughly a factor of two compared to those calculated by LAHET when optimized to reproduce the p/n ratios characteristic of high-Z materials, with iron-rich alloys in the 150–160 appm He/dpa range. This indicates that separate physics parameters are required for each range of atomic numbers. Finally, the ratio of ^{4}He/^{3}He generation appears to be somewhat sensitive to proton energy, increasing as the proton energy increases.

Hydrogen generation is roughly independent of composition and proton energy within the 500–800 MeV range, but there are energetic losses on the order of 50%, and diffusional losses that vary somewhat, depending on the solubility of hydrogen and the density and nature of both pre-existing and radiation-induced microstructural sinks. A surprisingly large fraction of the deposited hydrogen appears to be retained in all alloys tested during irradiation below 100°C. These retention rates indicate that the currently employed cross-sections for hydrogen generation do not need modification. Finally, if the irradiation-induced microstructural evolution is complicated, then the hydrogen retention will also exhibit complexity.

Acknowledgements

This work was supported by the US Department of Energy under the Accelerator Production of Tritium Program at Los Alamos National Laboratory. Battelle Memorial Institute operates Pacific Northwest National Laboratory for USDOE.

References

[1] APT ^{3}He Target/Blanket Topical Report, Los Alamos National Laboratory Report LA-CP-94-27, Rev. 1, Los Alamos National Laboratory, Los Alamos, NM, 1994.
[2] S.A. Maloy, W.F. Sommer, in: Proceedings of the Topical Meeting on Nuclear Applications of Accelerator Technology, Albuquerque, NM, November 16–20, 1997, p. 58.
[3] M.S. Wechsler et al., in: Second International Topical Meeting on Nuclear Applications of Accelerator Technology (AccApp '98), Gatlinburg, TN, September 20–23, 1998.
[4] H. Ullmaier, F. Carsughi, Nucl. Instrum. and Meth. B 101 (4) (1995) 406.
[5] S.L. Green, J. Nucl. Mater. 126 (1984) 30.
[6] F.A. Garner, L.R. Greenwood, B.M. Oliver, in: R.K. Nanstad, M.L. Hamilton, F.A. Garner, A.S. Kumar (Eds.), Effects of Radiation on Materials: 18th International Symposium, ASTM STP 1325, American Society for Testing and Materials, West Conshohocken, PA, 1999, p. 794.

[7] L.R. Greenwood, F.A. Garner, J. Nucl. Mater. 233–237 (1996) 1530.
[8] R.E. Prael, H. Lichtenstein, Los Alamos National Laboratory Report LA-UR-89-3014, Los Alamos National Laboratory, Los Alamos, NM, September 1989.
[9] J.J. Norgett, J.T. Robinson, I.M. Torrens, Nucl. Eng. Design 33 (1975) 50.
[10] H. Farrar, B.M. Oliver, J. Vacuum Sci. Technol. A 4 (1986) 1740.
[11] B.M. Oliver, J.G. Bradley, H. Farrar, IV, Geochimica et Cosmochimica Acta 48 (1984) 1759.
[12] B.M. Oliver, F.A. Garner, L.R. Greenwood, J.A. Abrefah, in: Proceeding of the Ninth International Conference on Fusion Reactor Materials, Colorado Springs, CO, October 10–15, 1999, J. Nucl. Mater. 283–287 (2000) 1006.
[13] M. Enke, C.M. Herbach, D. Hilscher, U. Jahnke, O. Schapiro, A. Letourneau, J. Galin, F. Goldenbaum, B. Lott, A. Peghaire, Nucl. Phys. A 657 (3) (1999) 317.
[14] S.L. Green, W.V. Green, F.H. Hegedus, M. Victoria, W.F. Sommer, B.M. Oliver, J. Nucl. Mater. 155–157 (1988) 1350.
[15] A. Gilbert, A.G.W. Cameron, Can. J. Phys. 43 (1965) 1446.
[16] A.V. Ignatyuk, G.N. Smirenkin, A.S. Tishin, Sov. J. Nucl. Phys. 21 (1975) 255.
[17] B.M. Oliver, M.L. Hamilton, F.A. Garner, W.F. Sommer, S.A. Maloy, P.D. Ferguson, in: M.L. Hamilton, A.S. Kumar, S.T. Rosinski, M.L. Grossbeck (Eds.), Effects of Radiation on Materials: 19th International Symposium, ASTM STP 1366, American Society for Testing and Materials, 2000, West Conshohocken, PA, p. 1109.
[18] B.H. Sencer, G.M. Bond, F.A. Garner, S.A. Maloy, W.F. Sommer, M.R. James, in: S.T. Rosinski, M.L. Grossbeck, T.R. Allen, A.S. Kumar (Eds.), Effects of Radiation on Materials: 20th International Symposium, ASTM STP 1405, American Society for Testing and Materials, West Conshohocken, PA, p. 2002.